Journal Name

ARTICLE TYPE

Cite this: DOI: 10.1039/xxxxxxxxxx

High-precision acoustic measurements of the non-linear dilatational elasticity of phospholipid coated monodisperse microbubbles†

Tim Segers*[a,b], Emmanuel Gaud[a], Michel Versluis[b], and Peter Frinking[a]

Received Date
Accepted Date

DOI: 10.1039/xxxxxxxxxx

www.rsc.org/journalname

The acoustic response of phospholipid-coated microbubble ultrasound contrast agents (UCA) is dramatically affected by their stabilizing shell. The interfacial shell elasticity increases the resonance frequency, the shell viscosity increases damping, and the nonlinear shell viscoelasticity increases the generation of harmonic echoes that are routinely used in contrast-enhanced ultrasound imaging. To date, the surface area-dependent interfacial properties of the phospholipid coating have never been measured due to the extremely short time scales of the MHz frequencies at which the microscopic bubbles are driven. Here, we present high-precision acoustic measurements of the dilatational nonlinear viscoelastic shell properties of phospholipid-coated microbubbles. These highly accurate measurements are now accessible for the first time by tuning the surface dilatation, that is, the lipid packing density, of well-controlled monodisperse bubble suspensions through the ambient pressure. Upon compression, the shell elasticity of bubbles coated with DPPC and DPPE-PEG5000 was found to increase up to an elasticity of 0.6 N/m after which the monolayer collapses and the elasticity vanishes. During bubble expansion, the elasticity drops monotonically in two stages, first to an elasticity of 0.35 N/m, and then more rapidly to zero. Integration of the elasticity vs. surface area curves showed that, indeed, a phospholipid-coated microbubble is in a tensionless state upon compression, and that it reaches the interfacial tension of the surrounding medium upon expansion. The measurements presented in this work reveal the detailed features of the nonlinear dilatational shell behavior of micron-sized lipid-coated bubbles.

1 Introduction

Ultrasound contrast agents (UCA) typically consist of suspensions of phospholipid-coated microbubbles with radii ranging from 1 to 5 μm that scatter ultrasound more efficiently than red blood cells and tissue owing to the large compressibility of the microbubble gas core.[1] The bubbles oscillate nonlinearly in response to a driving ultrasound field,[2] and the nonlinear echo allows for the visualization and quantification of organ perfusion.[3] The acoustic microbubble response is strongly dependent on the coupling between the ultrasound transmit frequency and the microbubble size through resonance.[4] The resonance frequency of a bubble is inversely proportional to its size. Moreover, the resonance behavior is strongly affected by the viscoelastic properties of the phospholipid shell.[2,5] First, during volumetric oscillations, energy is dissipated as a result of the intramolecular forces between the lipid molecules in the shell resulting in an increased damping.[6,7] Second, the microbubble resonance frequency is increased by the elasticity of the lipid shell. Shell elasticity χ results from surface tension gradients $d\sigma$, due to lipid packing density gradients, induced by the acoustically driven bubble-surface area variations dA: $\chi = Ad\sigma/dA$.[8]

Surface elasticity resulting from surface tension gradients during bubble oscillations, due to adsorbed surfactants was first considered by Glazman.[9] Later, in the context of UCA microbubbles, it was introduced by Sarkar *et al.*[10] and by Marmottant *et al.*[11] Both Rayleigh-Plesset type models include a pressure term that accounts for shell elasticity by assuming that the interfacial tension is linearly dependent on the bubble surface area. Thus, both models use a constant, bubble surface area independent, shell elasticity. However, Marmottant *et al.* limited the surface tension to zero for compressions beyond the buckling radius R_b, and to the surface tension of the surrounding medium for expansions beyond the rupture radius R_r, see the black curve in Fig. 1A. Therefore, purely elastic oscillations are limited to small amplitudes of oscillation around the initial bubble surface area A_0, see

[a] *Bracco Suisse S.A., Route de la Galaise 31, 1228 Geneva, Switzerland; E-mail: t.j.segers@utwente.nl*

[b] *Physics of Fluids group, TechMed Centre, MESA+ Institute for Nanotechnology, University of Twente, Postbus 217, 7500 AE Enschede, The Netherlands*

† Electronic Supplementary Information (ESI) available: [details of any supplementary information available should be included here]. See DOI: 10.1039/b000000x/

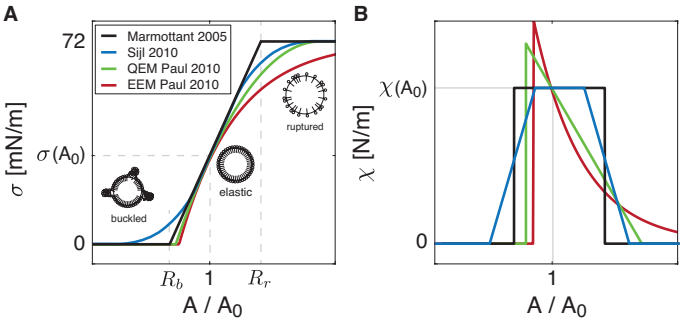

Fig. 1 (A) Schematic representation of several ad-hoc relations for the surface tension σ of a microbubble, with equilibrium surface area A_0, as a function of its normalized surface area A/A_0. (B) Shell elasticity χ resulting from the surface tension gradients: $\chi = Ad\sigma/dA$. These $\sigma(A/A_0)$ and $\chi(A/A_0)$ curves have been used in literature to model the dynamical response of a phospholipid coated microbubble to ultrasound.

Fig. 1B. The Marmottant model proved successful in describing non-linear dynamics of lipid coated bubbles[2] such as compression only[12] and subharmonics.[13,14] It has been shown that these non-linear phenomena are induced by the rapid change in the bubble shell elasticity with a small change in bubble surface area.[12,14] However, in the Marmottant model, the shell elasticity is incorporated in an unphysical way as it is discontinuous at the buckling and at the rupture radius, see Fig. 1B. Therefore, Sijl *et al.*[14] proposed to extend the Marmottant model with two cross-over functions for the transition from the regions with zero elasticity to the one with a finite elasticity, see the blue curves in Fig. 1. With the aim of getting closer to a more physicochemical surface area-dependent surface tension, i.e. with a decreasing elasticity for an increase in the area per lipid molecule, Paul *et al.*[5] tested a quadratic elasticity model (QEM) and an exponential elasticity model (EEM), see Fig. 1. They once again pointed out the importance of a surface area-dependent elasticity for non-linear bubble dynamics. However, to date, the $\sigma(A/A_0)$ dependence of a lipid-coated microbubble interface has never been measured due to the extremely short time scales and small length scales of ultrasound driven microbubble oscillations and, although very successful, it remains an ad-hoc assumption in the existing modeling effort without experimental justification.

The area-dependent interfacial tension of a flat lipid monolayer can be measured directly using a Langmuir trough[15] and that of a curved monolayer can be measured from the capillary pressure of a spherical cap-shaped bubble in a capillary pressure tensiometer.[16] However, using these common methods, surface area oscillations are limited to frequencies on the order of 10^2 Hz[17] whereas UCA bubbles oscillate at MHz frequencies. Furthermore, UCA bubbles are typically at least one order of magnitude smaller than the minimum cap radius in a bubble tensiometer[18] whereas the curvature of a monomolecular film may play a role in its viscoelastic properties.[17] Here, we present a novel experimental method to measure at high precision the nonlinear viscoelastic properties of micron sized phospholipid-coated bubbles as a function of their surface dilatation.

2 Measurement method

In order to measure the dilatational interfacial tension of the highly curved monomolecular phospholipid film self-assembled around a micrometric UCA bubble, the surface dilatation needs to be controlled while the interfacial tension is measured. Control over the surface dilatation, i.e. the phospholipid packing density, of a microbubble can be easily achieved by controlling the ambient pressure. However, a direct measurement of the interfacial tension of an UCA bubble is not possible at present. On the other hand, shell elasticity, as a local derivative of the interfacial tension with respect to the microbubble surface area, can be measured. To locally probe this derivative of the surface tension curve, small surface area oscillations are required to minimize the averaging of the surface area-dependent shell elasticity. Therefore, small-amplitude microbubble oscillations are required. The shell elasticity can be measured from these linear oscillations by fitting a harmonic oscillator model to the measured microbubble resonance curve.[5,19] When, at the same time, the surface dilation is controlled through ambient pressure control, the shell elasticity vs. surface area curve can be measured. Integration of the shell elasticity curve with respect to surface area then gives the surface area-dependent surface tension curve for phospholipid-coated UCA microbubbles.

The resonance curve of a single microbubble can be measured through microbubble spectroscopy using ultra high-speed imaging[7]. However, at the driving pressure amplitudes required to minimize the averaging of the surface area-dependent shell elasticity (< 5 kPa), the radial oscillations are on the order of 100 nm and these cannot be accurately resolved through optical imaging. On the other hand, the sensitivity offered by narrowband acoustic attenuation measurements can provide the complete frequency dependent resonance curve of a microbubble suspension insonified at low driving pressures.[20] Nevertheless, acoustic attenuation measurements can only be performed on a suspension of bubbles as the energy absorption of a single microbubble cannot be easily measured acoustically. A typical UCA consists of a suspension of polydisperse bubbles and since the resonance frequency of a microbubble is inversely proportional its size,[4] the attenuation spectrum of a polydisperse UCA is a complex superposition of the resonance curves of the individual microbubbles with different sizes and extraction of the dilatational elasticity and interfacial tension is therefore not feasible for a polydisperse bubble suspension.

Monodisperse bubble suspensions can be obtained by mechanical filtration[21], decantation[19], and centrifugation[22] of a polydisperse agent. Polydisperse bubbles can be sorted with a higher sorting precision in microfluidic devices, e.g., microbubbles can be sorted to size in a pinched microchannel[23] and they can be sorted to their acoustic property using the primary radiation force[24]. Monodipserse bubbles can also be synthesized directly in a microfluidic flow-focusing device.[25–27] Here, a gas thread is focused between two liquid flows through a narrow orifice where the gas thread destabilizes and pinches off to release monodisperse bubbles. It has been shown that phospholipid-coated microbubbles formed by flow-focusing are inherently unstable, and

prone to diffusive Ostwald ripening, until a final monodisperse size is reached.[28] Moreover, low bubble production frequencies and very specific phospholipid mixtures with molar PEG fractions of at least 10% were used to avoid bubble coalescence in the outlet of the flow-focusing device.[28–30] However, recently, the full parameter space for stable monodisperse phospholipid-coated microbubble synthesis was characterized and universal equations for the stabilization process and for the coalescence probability have been derived.[31] These equations allow for the selection of the lipid concentration and flow-rates at a given PEG molar fraction, PEG chain length, flow-focusing geometry, and bubble size in order to lower the bubble coalescence probability below a predefined coalescence percentage. As such, this new insight allows for the production of stable monodisperse bubble suspensions using different phospholipid formulations. Here, microbubbles formed by flow-focusing and coated by DPPC mixed with DPPE-PEG5000 at molar PEG percentages of 5.0%, 7.5%, and 10.0% were characterized by ambient pressure controlled attenuation measurements to determine their dilatational shell elasticity and dilatational interfacial tension.

3 Experimental and numerical procedures

3.1 Phospholipid formulations

In this study, 3 phospholipid formulations were used to synthesize monodisperse microbubbles with different shell compositions. DPPC was mixed with DPPE-PEG5000 at molar percentages of 5.0, 7.5, and 10.0% and at total lipid concentrations of 30, 20, and 15 mg/mL, respectively. The total lipid concentration was increased for decreasing molar PEG ratios to minimize bubble coalescence in the outlet of the flow-focusing device.[31] The aqueous lipid dispersions were prepared as described in our previous work, however, no co-solvents or viscosity increasing chemicals, e.g. propylene glycol and glycerol, were added as they are now known to degrade the stability of the final bubble suspension.[31]

3.2 Bubble production in a flow-focusing device

Figure 2A shows an image of the employed custom made flow-focusing device. The features were isotropically etched to a depth of 8 μm in two glass wafers (Micronit Technologies b.v., Enschede, The Netherlands) that were aligned and bonded together to form a cylindrical channel with a length of 30 μm and a depth of 16 μm in which the bubbles pinch off.

Bubbles were produced at C_4F_{10} gas (F2 Chemicals Ltd.) pressures ranging from 1.0 to 1.2 bars and at liquid co-flow rates ranging from 100 up to 150 μL/min. The gas pressure was controlled by a pressure regulator (Omega, PRG101-25) connected to a pressure sensor (Omega, DPG1000B-30G). The flow-rate of the lipid suspension was controlled by a mass-flow controller (mini CoriFlow, Bronkhorst Nederland B.V., The Netherlands) and its liquid reservoir was pressurized by C_4F_{10} gas. The outlet of the flow-focusing device was connected to a 24G needle via PEEK tubing (Upchurch) to facilitate the collection of the bubbles in a sealed glass vial that was pre-filled with pure C_4F_{10} gas, see Fig. 2B. A vent needle was pierced through the closing rubber stopper and it was positioned against the bottom of the glass vial that

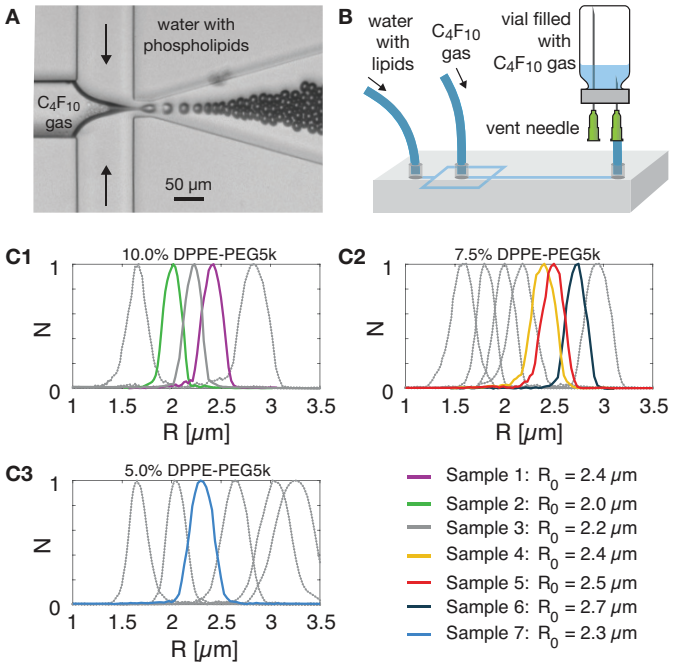

Fig. 2 (A) Image of the custom-made flow-focusing device used to produce C_4F_{10}-filled monodisperse microbubbles. (B) The bubbles were collected in a vial that was pre-filled with C_4F_{10} gas. (C) Size distributions of the bubble populations coated with (C1) 10.0 mol % PEG5000, (C2) 7.5 mol % PEG5000, and with (C3) 5.0 mol % PEG5000 that were characterized in this study.

was placed upside-down during bubble collection. Since C_4F_{10} gas has a higher density than air, it does not spontaneously drain from the vial. Bubbles were collected for 10 minutes after which the needles were removed. The vial was put to rest for 2 days to allow the bubbles to stabilize in the vial with its headspace filled with C_4F_{10} gas before acoustic characterization experiments were performed.[28] Within 1 hour before the start of an attenuation experiment, the bubble size distribution was measured using a Coulter counter (Multisizer 3, 30 μm aperture tube, Beckman Coulter, Brea, CA, USA) at a dilution factor of 1:2000 in saline. Figure 2C shows the size distributions of the bubble samples with a typical polydispersity index of 5 to 6% (PDI: standard deviation divided by the mean radius) that were characterized in this study. The bubble concentrations ranged from 200 to 350 million bubbles/mL.

3.3 Ambient pressure dependent acoustic characterization

The resonance behavior of the microbubble populations with the colored size distributions, Fig. 2C, were characterized by attenuation measurements at a rate of 10 s^{-1} at ambient pressures ranging from 60 kPa to 145 kPa. Before the measurement, 30 μL of bubble suspension was diluted in a beaker filled with 150 mL air-saturated saline (5000$\times$ dilution). The diluted mixture was homogenized by stirring for a duration of 20 s using a magnetic stirrer. Then, part of the mixture was poured into the filling reservoir of the acoustic characterization setup and its sample container (Fig. 3B) was filled through gravity, see Fig. 3A. The sam-

ple container was custom-made from a Perspex cylinder with an inner diameter of 35 mm and a width of 9 mm (d in Fig. 3B). It was sealed by two acoustically transparent polyester membranes with a thickness of 80 μm (Melinex, DuPont Teijin Films, Chester, VA) that were glued and clamped on both sides of the Perspex cylinder by Perspex rings. A magnetic stirrer bar placed inside the container ensured a homogeneous bubble suspension during the measurement. The sample container was air and water tight and two 5 mm tube connections, one at the top and one at the bottom (Fig. 3B), were used to fill, empty, and pressurize the sample container. During the filling procedure, the T-valves were positioned as indicated by the black T-shaped symbols in Fig. 3A. After filling, the valves were positioned such that a closed circuit was formed, see green T-shaped symbols in Fig. 3A. The static pressure in the closed circuit was controlled through air compression and decompression using an air-filled 60 mL syringe mounted on a syringe pump (PHD 4400, Harvard Apparatus, Holliston, MA) that was operated at a constant flow-rate of +90 mL/min or -90 mL/min, respectively. Every microbubble sample was characterized by two measurements. First, the ambient pressure was lowered from atmospheric pressure down to 60 kPa for a duration of 11 s resulting in 110 attenuation spectra. Then, the sample was refreshed and the ambient pressure was increased from atmospheric pressure up to 145 kPa for a duration of 11 s, again resulting in 110 attenuation spectra.

Attenuation measurements were performed at room temperature using two transducers that were confocally aligned within the bubble container, see Fig. 3A. The transmit signals were narrowband 12-cycle sinusoidal pulses with a half-Gaussian tapering over 2 cycles on both sides of the pulse to minimize transient effects at transmit frequencies close to the boundaries of the transmit transducer bandwidth. The transmit transducer (V304, Panametrics-NDT, Waltham, MA) had an aperture of 25.4 mm, a focal distance of 76.2 mm and a center frequency of 2.25 MHz. The -6 dB focal length of the transmit transducer was 2 to 4 cm (5.7 MHz to 1.0 MHz, respectively), i.e. it was larger than the intersection of the acoustic beam with the sample container to ensure a homogeneous acoustic pressure and nearly plane waves in the sample container. The frequency of the transmit pulses was varied from 0.7 MHz to 5.7 MHz in steps of 0.1 MHz. At each frequency, attenuation was measured from a single 12-cycle transmit pulse.[28] The frequency-dependent output of the transmit transducer was measured for the 12-cycle driving pulses transmitted at all employed driving frequencies using a calibrated membrane hydrophone (MH026, Precision Acoustics Ltd., Dorset, UK). The measured response was used to correct the transducer driving voltage such that the acoustic focal pressure was 5 kPa over the full transmit frequency-range. The transmit pulses were generated by an arbitrary waveform generator AWG1 (LeCroy, Arbstudio 1104) that was programmed before the measurements. A second waveform generator AWG2 (8024, Tabor, Tel-Hanan, Israel) triggered AWG1 by a burst of 51 pulses at a rate of 5 kHz to record a complete attenuation spectrum in 10.2 ms. AWG2 was triggered by a third waveform generator AWG3 (8024, Tabor, Tel-Hanan, Israel) at a rate of 10 Hz to measure a full attenuation spectrum every 100 ms. The transmitted signals were amplified

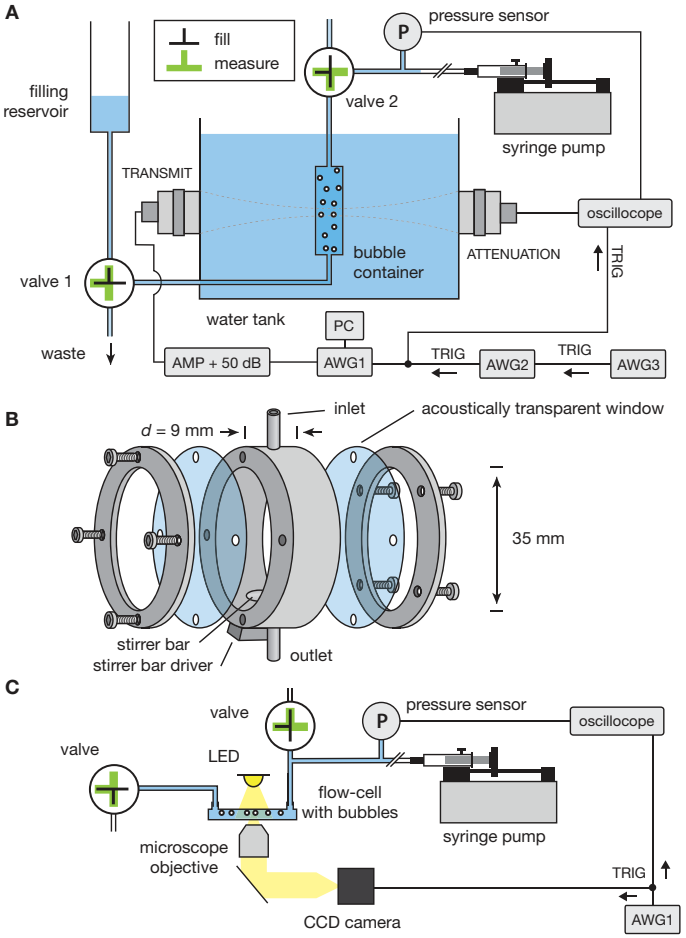

Fig. 3 (A) Schematic representation of the setup designed to characterize microbubble suspensions through attenuation measurements at absolute ambient pressures ranging from 60 to 145 kPa. (B) Detailed schematic of the bubble sample container. (C) Setup to optically measure ambient pressure-dependent microbubble size.

by a 55 dB linear power amplifier (ENI, 3200 L, ENI, Rochester, NY) and received by the transducer (M3, 3 MHz, 110% -6 dB relative bandwidth, Vermon, Tours, France) in line with the transmit transducer. The received signals were recorded by an oscilloscope (LeCroy, HRO 64Zi) operated in sequence acquisition mode at a sampling rate of 50 MHz. The oscilloscope was triggered by AWG2 and at each trigger pulse it recorded both a time trace of the attenuated transmit signal and the output voltage of the pressure sensor (Almemo 2290-2).

Due to the limited bandwidth of the transmit and receiving transducers, only a narrow range of bubble sizes could be characterized by ambient pressure-dependent attenuation measurements, see the colored size distributions in Fig. 2C. In a second experiment performed at atmospheric pressure alone, all bubble samples with the size distributions shown in Fig. 2C were characterized by attenuation measurements at a peak negative acoustic pressure of 5 kPa. These measurements were performed to obtain shell parameters at atmospheric pressure over a larger bubble size-range and to compare them with the ambient pressure-dependent results. The bubble-sample handling and dilution fac-

tor were as before.

3.4 Optical ambient pressure-dependent bubble size measurement

In a separate experiment, the bubble size was measured optically as a function of the ambient pressure using a CCD camera (LM165M, Lumenera, 6.45 μm pixel size) connected to a microscope (Olympus IX50), see Fig. 3C. The microscope was equipped with a 40× objective (Olympus LCPlanFl) resulting in an optical resolution of 0.16 μm/pixel. The bubble samples were diluted by 20 times and infused in a flow-cell (IBIDI μ-slide) with a 100 μm channel height that was positioned in the field of view of the microscope objective. The ambient pressure in the flow cell was controlled using a syringe pump, as before. A waveform generator AWG1 (8024, Tabor, Tel-Hanan, Israel) was used to simultaneously trigger the camera and the oscilloscope (LeCroy, HRO 64Zi). The oscilloscope was operated in sequence mode to record the output voltage of the pressure sensor at a rate of 10 s^{-1}. During the pressure measurement, the ambient pressure in the flow cell was decreased in a first measurement from atmospheric pressure down to 60 kPa using the syringe pump, as before. The bubble size was recorded optically also at a rate of 10 s^{-1} using the camera. In a second measurement, using a fresh bubble sample, the ambient pressure was increased from atmospheric pressure to 145 kPa.

3.5 Data analysis

Attenuation curves were processed using MATLAB (The MathWorks, Inc., Natick, Massachusetts, US). For each transmit frequency f_T, the corresponding time trace was first gated by a window with a temporal length equal to that of the 12-cycle transmit pulse at f_T. The window was delayed by 102 μs with respect to the start of the transmit pulse, this was the travel time of the ultrasound wave from the transmit transducer to the receiving transducer. The windowed signals were then bandpass-filtered between 100 kHz and 10 MHz using a fourth order Butterworth filter, after which the power spectrum was calculated. The attenuation coefficient α at transmit frequency f_T was calculated from the amplitude of the power spectrum at f_T obtained from a measurement with bubbles present and from that of a reference measurement without bubbles present, as follows:

$$\alpha_{exp} = -\frac{10}{d} log_{10} \frac{|V_{bub}(f_T)|^2}{|V_{ref}(f_T)|^2}, \tag{1}$$

where $|V_{bub}(f_T)|^2$ and $|V_{ref}(f_T)|^2$ are the amplitudes of the power spectra obtained from the time traces recorded with and without bubbles present at transmit frequency f_T, respectively, and where d is the acoustic path length over which bubbles are present.

The optical microscope recordings were processed frame by frame with an automated image processing algorithm written in Matlab.[24] For all bubbles in the image, first, the center of the bubble was found from a processed binary image. Then, the original bubble image was transformed into polar coordinates with the bubble center at the origin. The intensity profile of the bubble was averaged over all angles and the bubble size was determined from the inflection point of the average intensity profile. The bubble position data and its size were stored in a matrix, and a tracking algorithm[32] was used to identify bubbles over the different frames such that the ratio $R(P_{amb})/R_0$ could be determined for each bubble, with R_0 the bubble size at atmospheric pressure.

3.6 Bubble dynamics: modeling the attenuation spectra

Several models are available for modeling non-linear bubble dynamics.[5,10,11] Here, we use the modified Rayleigh-Plesset type equation given by Marmottant et al.:[11]

$$\rho\left(\ddot{R}R+\frac{3}{2}\dot{R}^2\right) = \left(P_0+\frac{2\sigma(R_0)}{R_0}\right)\left(\frac{R_0}{R}\right)^{3\kappa}\left(1-\frac{3\kappa\dot{R}}{c}\right) - P_0 - P_A(t) - \frac{2\sigma(R)}{R} - \frac{4\mu\dot{R}}{R} - \frac{4\kappa_s\dot{R}}{R^2}, \tag{2}$$

where ρ is the liquid density, μ the liquid viscosity, c the speed of sound in the liquid, κ the polytropic exponent of the gas inside the bubble, with P_0 the ambient pressure and P_A the acoustic driving pressure. R_0 is the initial bubble radius, R the time-dependent radius of the bubble and the overdots denote its time derivatives. κ_s accounts for the dilatational viscosity of the shell. The effective surface tension is captured by $\sigma(R)$.

The Rayleigh-Plesset type equation, Eq. 2, can be linearized to describe bubble dynamics at small amplitudes of oscillation around the equillibrium radius R_0. The radial amplitude of oscillation is given by:[4]

$$R_\varepsilon = \frac{P_A}{R_0\rho}\frac{1}{\sqrt{(\omega_0^2-\omega^2)^2+(\delta_{tot}\omega_0\omega)^2}} \tag{3}$$

where $\omega = 2\pi f_T$ is the angular ultrasound frequency, and ω_0 the angular eigenfrequency that is given by:[7]

$$\omega_0 = \sqrt{\frac{1}{\rho R_0^2}\left(3\kappa P_0 + (3\kappa-1)\frac{2\sigma(R_0)}{R_0} + \frac{4\chi}{R_0}\right)}, \tag{4}$$

with $\chi = Ad\sigma/dA$ the shell elasticity at the equilibrium bubble radius R_0. The corresponding dimensionless damping coefficients are given by:[4]

$$\delta_{rad} = \frac{3P_0\kappa}{\rho\omega c R_0} \approx \frac{\omega R_0}{c}, \qquad \delta_{vis} = \frac{4\mu}{\rho\omega R_0^2}, \qquad \delta_{shell} = \frac{4\kappa_s}{\rho\omega R_0^3}. \tag{5}$$

where δ_{rad} the damping due to the re-radiation of ultrasound, δ_{vis} the damping resulting from the liquid viscosity, and δ_{shell} the shell viscous damping. A microbubble also experiences thermal damping δ_{th} due to heat diffusion[4,33] and since for UCA bubbles it is of the same order as the viscous damping for a bubble in water,[4] typically the viscosity of the medium is increased by a factor 2 to account for thermal damping.[14,20] The total damping: $\delta_{tot} = \delta_{rad} + \delta_{th} + \delta_{vis} + \delta_{shell}$, results in a slightly reduced microbubble resonance frequency ω_{res} as compared to its eigenfrequency ω_0, as follows:

$$\omega_{res} = \omega_0\sqrt{1-\frac{\delta_{tot}^2}{2}} \tag{6}$$

Moreover, damping results in energy loss of the insonifying acoustic wave. The energy loss of a driving ultrasound wave with angular frequency $\omega = 2\pi f_T$ resulting from scattering, or re-radiation of ultrasound, from a single microbubble can calculated from the scattering cross-section, which for small amplitudes of oscillation can be expressed as:[4,34]

$$\Omega_{scs} = \frac{4\pi R_0^2}{((\omega_0/\omega)^2 - 1)^2 + \delta_{tot}^2}. \quad (7)$$

The total amount of scattered and absorbed energy of an acoustic wave propagating through a dilute cloud of homogeneously distributed bubbles at concentration n can be obtained by summation over the scattering- and extinction cross-sections of all the individual bubbles present in the acoustic beam[34] when higher order scattering effects are negligible, i.e. when $n^{2/3}\Omega_{scs} \ll 1$.[19,35]

The total attenuation α_{model} of an ultrasound wave traveling trough a bubble suspension is a result of the total energy dissipation resulting from the presence of bubbles and it is given by:

$$\alpha_{model} = -\frac{10}{ln(10)} \sum_R \frac{\delta_{tot}}{\delta_{rad}} n(R)\Omega_{scs} d, \quad (8)$$

with $n(R)$ the bubble size dependent bubble concentration, and d the acoustic path length over which the sound wave interacts with the bubbles.

3.6.1 The fitting procedure: obtaining the shell parameters

Equations 4-8 were used to obtain shell elasticity and shell viscosity as function of ambient pressure by fitting a modeled attenuation curve α_{model} to every experimentally measured attenuation curve α_{exp}.[10,36–38] First, the bubble size distribution measured at atmospheric pressure was multiplied by the optically measured average ambient pressure-dependent bubble-size-change ratio $R(P_{amb})/R_0$ of the considered bubble sample to find the bubble size distribution at ambient pressure P_{amb}. Then, for each bubble size in the size distribution, the resonance frequency was calculated using Eq. 4 using an initial set of shell parameters; χ = 0.5 N/m and $\kappa_s = 1 \times 10^{-8}$ kg/s. Further input parameters to Eq. 4 were the liquid density ρ = 1000 kg/m^3, the speed of sound c = 1500 m/s, the polytropic exponent of the C_4F_{10} gas κ = 1.07, and the initial surface tension $\sigma(R_0)$ that was set to 0.035 N/m during the first run of the fitting procedure. Subsequently, the dimensionless damping constants were calculated using Eq. 5 for each bubble size in the size distribution and for every experimentally employed insonation frequency f_T. The viscosity of the water $\mu = 1$ mPa·s was increased by a factor of 2 to account for thermal damping.[14] Next, the scattering cross-section given by Eq. 7 was calculated in order to calculate a modeled attenuation spectrum using Eq. 8. The modeled attenuation spectrum α_{model} was compared to the experimentally measured attenuation spectrum α_{exp} through the root-mean-square (RMS) error defined as follows:

$$RMS = \sqrt{\sum (\alpha_{exp} - \alpha_{model})^2}. \quad (9)$$

The RMS error was minimized using the *fminsearch* function in MATLAB to find a best fit for the shell elasticity and the shell viscosity for each experimentally measured attenuation curve. The interfacial surface tension was then calculated by numerical integration of the shell elasticity, as follows:[8]

$$\sigma(A) = \int_0^A \frac{\chi(A)}{A} dA. \quad (10)$$

The obtained $\sigma(A)$ curve was entered in a second run of the fitting procedure now having a better estimation for $\sigma(R_0)$ in Eq. 4, i.e. $\sigma(R_0) = \sigma(R(P_{amb}))$. Then, the fitting procedure was repeated and each time, $\sigma(A)$ obtained during run number n was input to the next run $n+1$, and so on, until the $\sigma(A)$ curve converged, i.e. until the root-mean-square error with respect the previous run was below 10^{-5}.

4 Results and discussion

A typical ambient pressure-dependent attenuation measurement is shown in Fig. 4A. It shows a surface plot of the 220 attenuation spectra measured for Sample 1 (Fig. 2C) with an initial bubble radius of 2.4 μm (at atmospheric pressure). A movie of the individual attenuation spectra changing with the ambient pressure variation can be found in the supplementary information. The bubbles were coated with a mixture of DPPC and 10 mol % DPPE-PEG5000. The frequency of maximum response f_{MR} of the attenuation spectra in Fig. 4A as a function of the ambient pressure P_{amb} is plotted in Fig. 4B. Starting at atmospheric pressure, a decrease in P_{amb} results in a decrease of the f_{MR}. The other way around, an increase of P_{amb} results in an increase of the f_{MR} up to a certain ambient pressure, 124 kPa in this case, where after the f_{MR} suddenly drops.

The ambient pressure-dependent bubble radius was measured directly using optical microscopy and it is shown in Fig. 4C for Sample 1. The smoothed data (solid red line) was used in the fitting procedure as described before to obtain the shell elasticity and the shell viscosity as a function of P_{amb}. To demonstrate the robustness of the fitting procedure, Fig. 4D shows modeled attenuation curves (solid lines) that were fitted to 5 out of the 220 measured attenuation curves (dots) shown in Fig. 4A. The fitting procedure was performed for all measured attenuation spectra shown in Fig. 4A. The product $n^{2/3}\Omega_{scs}$ was 0.024 at maximum, confirming that multiple scattering could be neglected in the modeling.

Figure 4E shows the obtained shell elasticity as a function of the normalized bubble surface area A/A_0, with A_0 the surface area of the bubble at atmospheric pressure. It shows that, upon compression, the elasticity of the phospholipid shell increases up to 0.6 N/m where a maximum compression is reached. Upon further compression, the monolayer collapses, or buckles, and the shell elasticity drops to zero. When the monolayer is compressed even further, the shell elasticity jumps back up to higher values (red crosses) indicating the loss of shell material through, e.g. lipid shedding.[39,40] Therefore, these data points are excluded for further analysis. Upon expansion, the shell elasticity decreases, first gradually to 0.35 N/m, and then more rapidly, to zero.

To measure the rigor of the bubble stability, a second ambient pressure-dependent attenuation measurement was performed on Sample 1. The bubble sample was refreshed and subsequently,

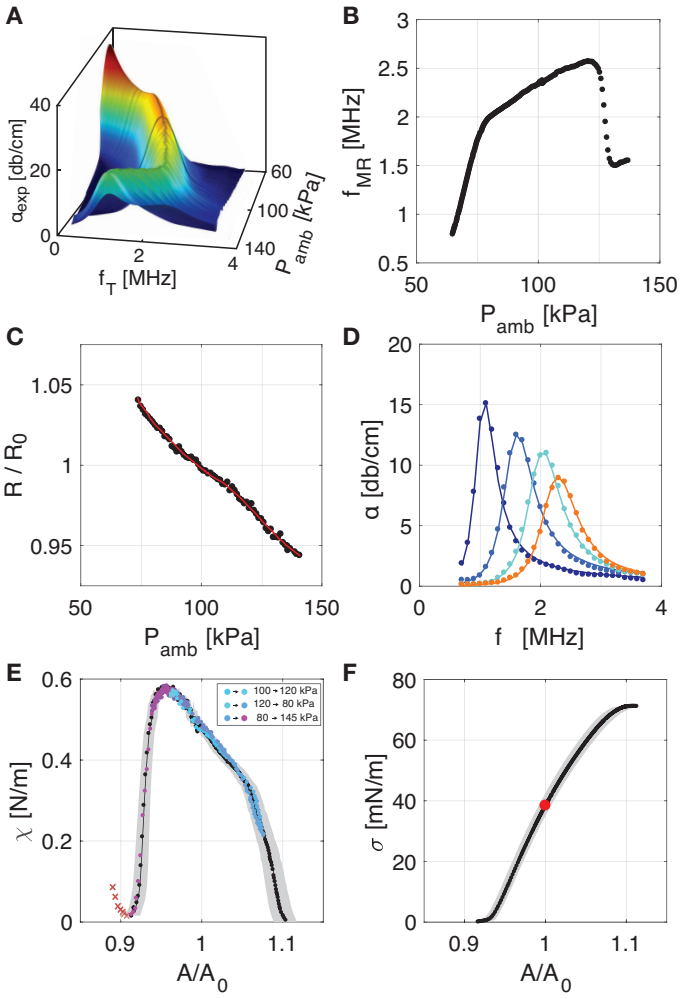

Fig. 4 (A) Surface plot of the 220 attenuation curves measured at absolute ambient pressures ranging from 60 to 145 kPa for microbubble Sample 1. (B) The frequency of maximum response f_{MR} of the attenuation curves shown in (A) as a function of the ambient pressure. (C) Optically measured ambient pressure dependent bubble size. (D) A linear model (solid lines) was fitted to the measured attenuation curves to obtain the shell elasticity χ (E). The gray area represents the error. (F) The obtained shell elasticity was integrated using Eq. 10 to obtain the interfacial tension as a function of the bubble surface area A normalized to the bubble surface area at atmospheric pressure A_0.

the ambient pressure was increased from atmospheric pressure to 120 kPa, then down to 80 kPa, and finally all the way up to 145 kPa. The obtained shell elasticity from this second measurement is also plotted in Fig. 4E (colored dots). The light blue dots represent the start of the measurement and the dark purple ones the end of the P_{amb} cycle, see legend. The $\chi(A/A_0)$ data collapses on the same curve as the data obtained from the first two measurements; one from atmospheric pressure down to 60 kPa, and one from atmospheric pressure up to 145 kPa (black dots) indicating that the bubbles were highly stable during the pressure cycle as loss of shell material through lipid shedding,[39,40] or a change in bubble size due to gas diffusion, would have resulted in a different $\chi(A/A_0)$ curve. Thus, the bubble size changed only due to mechanical compression and decompression of the bubble/gas system.

To quantify the shell elasticity, the microbubble surface area needs to oscillate. These surface area oscillations effectively average the shell elasticity over the imposed variation in surface area. To estimate the corresponding error in the obtained shell elasticity, Eq. 3 was used to calculate the magnitude of the acoustically driven surface-area oscillations during the attenuation measurement. The lower area-limit of the gray area plotted in Fig. 4E represents $(R-R_\varepsilon)^2/R_0^2$ and the upper limit $(R+R_\varepsilon)^2/R_0^2$. At the frequency of maximum response, the measured attenuation levels were at least 20 dB/cm, see Fig. 4A, i.e, the driving acoustic pressure wave decreased in amplitude by at least 90% after passing through the bubble sample.[41] Thus, the deliberately chosen high bubble concentrations, resulting in high attenuation levels, effectively lowered the average acoustic pressure amplitude by which the bubbles were driven to 2.7 kPa and this value was used in Eq. 3 together with δ_{tot} and ω_0 obtained directly from the model fit. The narrowness of the gray area in Fig. 4E points out the high accuracy of the novel elasticity measurement technique presented in this work.

The shell elasticity of Fig. 4E was numerically integrated following Eq. 10 to obtain the normalized bubble surface area-dependent interfacial tension $\sigma(A/A_0)$, see Fig. 4F. The constant of integration was zero and integration was started at the area A where χ reached its minimum value during compression (at $A/A_0 = 0.91$ in Fig. 4E). Figure. 4F shows that for a compressed bubble, the surface tension is zero and it increases, first more rapidly and later more slowly, with an increase in bubble surface area to the surface tension of the surrounding water. Since the initial surface area A_0 is known from the optically measured bubble size, the surface tension at atmospheric pressure, i.e. the initial surface tension $\sigma(A_0)$ is known. $\sigma(A_0)$ is indicated by the red dot in Fig. 4F and it was 38 mN/m. The relatively high initial surface tension is discussed below where Fig. 5D is introduced.

To investigate the universality of the measured shell elasticity and surface tension curves with varying PEG molar fraction and bubble sizes, the measurements were repeated for 6 other bubble populations with DPPE-PEG5000 molar concentrations of 5.0%, 7.5%, and 10.0% and with mean bubble radii ranging from 2.0 μm to 2.7 μm, see Samples 2−7 in Fig. 2C. Figure 5A shows the optically measured ambient pressure-dependent normalized bubble radius R/R_0, smoothed over 5 points, that was used in the fitting procedure together with the measured attenuation spectra (not shown but similar to Fig. 4A). Bubbles of a different size, or bubbles originating from different samples, may have a different lipid packing density at atmospheric pressure, i.e. a different $\sigma(A_0)$, resulting in a mutual shift of the elasticity curves towards a higher or a lower normalized surface area A/A_0. Therefore, to allow for a comparison between the different samples, the bubble surface area A is now normalized by its surface area A_N at a surface tension σ of 40 mN/m, instead of its surface area at atmospheric pressure A_0. A surface tension of 40 mN/m was selected since it is close to the initial surface tension of Sample 1. To obtain A_N, the shell elasticity curves were first integrated according to Eq. 10 to obtain $\sigma(A)$, from which then A_N was determined. The shell elasticity obtained from the fitting procedure is plotted

in Fig. 5B as a function of A/A_N for bubble Samples 1−7. All data collapses on a single curve showing that shell elasticity is only dependent on the area per lipid molecule, and not on bubble size. Moreover, for the DPPE-PEG5000 molar fractions used here, no difference is observed in the bubble surface area dependent shell elasticity.

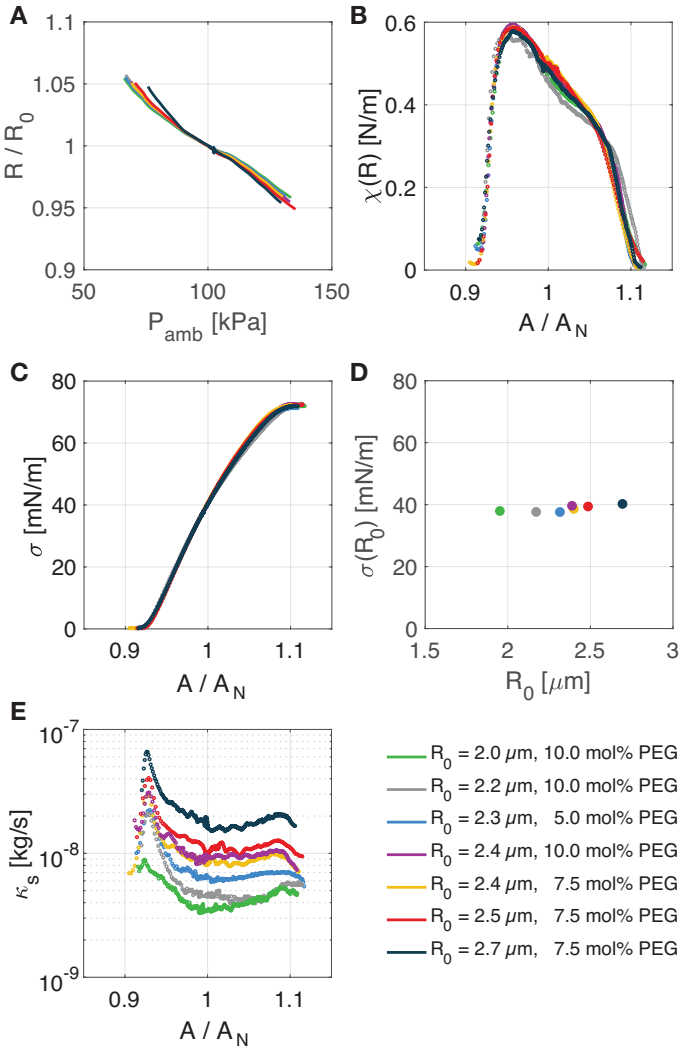

Fig. 5 (A) Optically measured ambient pressure-dependent bubble size for the colored size distributions shown in Fig. 2C. (B) Shell elasticity as a function of the bubble surface area A normalized to A_N; the bubble surface area at a surface tension of 40 mN/m. (C) The shell elasticity curves in (B) were integrated using Eq. 10 to obtain the surface tension as a function of A/A_N. (D) Initial surface tension as a function of the microbubble radius at atmospheric pressure R_0. (E) Shell viscosity as a function of A/A_N.

Figure 5B shows that the shell elasticity of a lipid coated microbubble depends on the lipid packing fraction. Thus, the shell elasticity of microbubbles in suspension, either stored in a vial or in dilution, may vary over time due to the loss of gas resulting in a lower equilibrium surface tension $\sigma(A_0)$. Nevertheless, Fig. 5B shows that this potential variation in shell elasticity does not necessary imply a change in the molecular composition of the microbubble coating.

As before, the interfacial surface tension is found by integration of the $\chi(A)$ curves shown in Fig. 5B by using Eq. 10. It is plotted in Fig. 5C as function of A/A_N. All $\sigma(A/A_n)$ curves collapse on a single curve. This again demonstrates that the surface tension of a lipid coated microbubble depends purely on its surface area per lipid molecule and not on absolute bubble size / surface area.

The initial surface tension $\sigma(A_0)$ is plotted in Fig. 5D as a function of the bubble radius R_0 at atmospheric pressure. For all bubble samples, $\sigma(R_0)$ is close to 40 mN/m. This value is surprisingly high since it is expected that a higher lipid packing fraction results in a more stable bubble, and that therefore, the initial surface tension of a phospholipid-coated bubble naturally decreases to values close to zero.[42,43] Moreover, initial surface tension values reported in literature are mostly at or below 20 mN/m.[2,12]

As a self-consistent check of the $\sigma(R)$ curve and the $\sigma(R_0)$ values, $\sigma(R)$ was directly obtained from an optically measured $R(P_{amb})$ curve (Fig. 4C) using the polytropic gas law ($PV^\gamma = const.$) and from the gas pressure inside the bubble, as follows: $\sigma(R) = R/2((P_0 + 2\sigma(R_0)R_0^{-1})(R_0R^{-1})^{3\gamma} - P_{amb})$, where R is the measured ambient pressure dependent bubble radius, P_0 atmospheric pressure, R_0 the bubble radius at atmospheric pressure and γ the polytropic exponent that was set to 1 for the relatively slow and thus isothermal compression and expansion. The $\sigma(R_0)$ was set to 40 mN/m, such that the obtained $\sigma(R)$ curve had values between zero and the surface tension of water. The obtained dilatational σ and χ curves were found to be noisy (see Fig. S1, supplementary information) however, the trends were consistent with those obtained from the attenuation measurements. Furthermore, the value of $\sigma(R_0)$ was equal to that obtained using the attenuation measurements. The high initial surface tension found in this work may be related to the microbubble collection method, i.e. in a vial filled with pure C_4F_{10} gas. It may also be related to the long PEG5000 surface-grafted polymer in the microbubble shell, on which no characterization is presently available in literature. The relatively high initial surface tension in combination with the high microbubble stability suggests a high resistance of the microbubble shell against gas transport through the shell membrane.[44] Nevertheless, the exact nature of the high initial surface tension values found in this work remains unexplained and should be subject of future studies.

For the DPPE-PEG5000 molar fractions used here (5 - 10%), no difference is observed in the bubble surface-area dependent shell elasticity (Fig. 5B). Lozano and Longo[15] measured surface pressure-area isotherms for DPPC/DSPE-PEG2000 mixtures and they also found very little variation in surface pressure between DPPC monolayers with DSPE-PEG2000 molar fractions of 5 to 10%. From Lozano and Longo's data, larger differences can be expected for lower PEG molar fractions. Indeed, Dicker *et al.*[45] showed an increased shell stiffness for bubbles coated with only 1 mol % of DSPE-PEG5k as compared to bubbles coated with 7.5 mol % DSPE-PEG5k (mixed with DSPC). However, in practice it will be very challenging to produce stable monodisperse microbubbles at high-production rates by flow-focusing using an even lower PEG molar fraction than 5% since this results in severe coalescence of the formed bubbles, unless total lipid concentrations on the order of 10^2 mg/mL are used.[31] Therefore, tuning

the acoustic response of microbubbles formed by flow-focusing through a variation of the PEG molar fraction seems a non-viable route.

The shell viscosity κ_s as a function of P_{amb} was also obtained from the fitting procedure and it is plotted in Fig. 5E as a function of A/A_N. While the shell viscosity curves for the bubbles with different sizes (see legend) are of similar shape, the average κ_s increases with increasing bubble radius, as expected from literature.[7,46,47] With regard to the shape of the curves, starting at atmospheric pressure, κ_s is relatively constant for a decrease in ambient pressure. However, when the bubble is compressed, κ_s substantially increases. The increase in shell viscosity at higher lipid packing densities and surface pressures may result from the larger intermolecular forces at these smaller intermolecular distances. An increase in dilatational surface viscosity with an increasing surface pressure was also observed in macroscopic oscillating pendant drop and bubble tensiometry experiments.[48,49] Furthermore, motivated by in-vivo blood pressure variations, Kumar *et al.* measured shell properties at overpressures up to 200 mm Hg (27 kPa).[50] For Definity bubbles with a very similar shell composition to the 10% PEG lipid mixture used here, Kumar et al.[51] also found a shell viscosity and shell elasticity increase for increased ambient pressures.

In the second experiment a total of 19 different monodisperse bubble populations with mean bubble radii ranging from 1.6 μm to 3.2 μm (see size distributions in Fig. 2C1-3), were characterized by attenuation measurements at atmospheric pressure and at a peak negative acoustic pressure of 5 kPa. The obtained shell elasticity is shown in Fig. 6A. As before, it is shown to be independent of the bubble size and the average value is 0.53 N/m, in perfect agreement with $A/A_N = 1$ in Fig. 5B. The obtained shell viscosity is shown in Fig. 6B. The shell viscosity κ_s increases with bubble size as was reported before.[7,46,47] Bubble size-dependent shell viscosity may result from a dependence of κ_s on dilatation rate.[7] Attempts have been made to include a dilatation rate dependent κ_s in the modeling of bubble dynamics, however, at the cost of an extra fitting parameter.[52] At present, a physical model for a dilatation-rate dependent κ_s is still missing. Here, we focus on shell elasticity and surface tension and dilatation rate dependent shell viscosity is beyond the scope of the present work. As for the shell elasticity, the obtained shell viscosity values are independent of the DPPE-PEG5000 molar faction in the range of 5 to 10%.

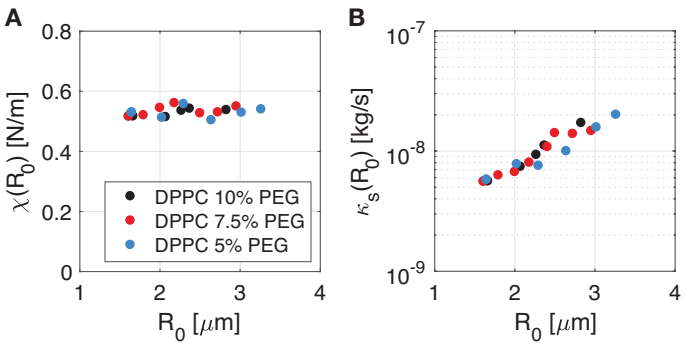

Fig. 6 (A) Shell elasticity and (B) shell viscosity at the equilibrium bubble radius R_0 measured for bubbles coated by DPPC and DPPE-PEG5000 mixed at molar PEG ratios of 5.0%, 7.5%, and 10.0%.

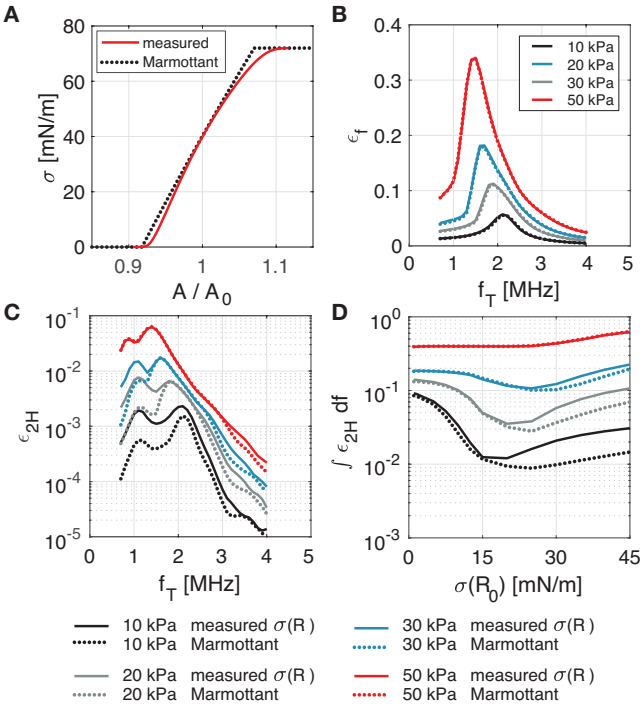

Fig. 7 (A) The full nonlinear Rayleigh-Plesset type model, Eq. 2, was solved for peak negative acoustic pressures of 10, 20, 30, and 50 kPa using the measured $\sigma(A/A_0)$ relation and using the Marmottant model. (B) There is no significant difference between the modeled radial amplitude of oscillation at the fundamental frequency ε_f using both $\sigma(A/A_0)$ relations. (C) At the second harmonic, the relative radial amplitude of oscillation modeled using both $\sigma(A/A_0)$ relations shows a higher response below resonance for that modeled using the measured $\sigma(A/A_0)$ curve. (D) Total radial amplitude of oscillation at the second harmonic as a function of the initial surface tension $\sigma(R_0)$.

The difference between bubble dynamics modeled using the Marmottant model, and that modeled using the $\sigma(A/A_N)$ curve measured in the present work was investigated by solving the full non-linear Rayleigh-Plesset equation (Eq. 2) for both cases. To that end, the average of the 7 measured interfacial surface tension curves (Fig. 5C) was parameterized. To capture all the details of the measured $\sigma(A/A_N)$ curve, i.e. in particular the rapid changes of its derivative (shell stiffness) around the buckling radius, a 10th degree polynomial fit was used, see solid red line in Fig. 7A. The initial surface tension was set to 40 mN/m, similar to what was obtained from the measurements presented in this work. The parametrization of $\sigma(A/A_N)$ can be found in Appendix 1. The shell elasticity χ in the Marmottant model was set to match the measured $\chi(A/A_0)$ at $A/A_0 = 1$, i.e. χ=0.5 N/m. Further input parameters to the model were an 8-cycle acoustic driving pulse, the density of water $\rho = 1000$ kg/m^3, atmospheric pressure $P_0 = 100$ kPa, the polytropic exponent for C_4F_{10} gas $\kappa = 1.07$, the speed of sound $c = 1500$ m/s, the equilibrium bubble size R_0=2.5 μm, and the viscosity of water $\mu = 1$ mPa·s. The

modeled amplitude of oscillation of the microbubble at the fundamental frequency relative to the initial bubble radius ε_f, found from the Fourier transformed radial response curves, is plotted in Fig. 7B for peak negative acoustic pressures of 10, 20, 30, and 50 kPa. The frequency of maximum response shifts to a lower frequency with an increasing driving pressure due to the effective averaging of the shell elasticity over elastic and nonelastic regions.[2,20,41,53,54] The microbubble surface area over which the bubble has a finite stiffness is relatively small and therefore, at high driving pressures, the bubble essentially resonates at the frequency of an uncoated gas bubble. No difference is observed between the amplitude of oscillation at the fundamental frequency modeled using the Marmottant model (dots) and the $\sigma(A/A_0)$ curve measured in this work (solid lines). However, at the second harmonic, the relative amplitude of oscillation ε_{2H} modeled using the $\sigma(A/A_0)$ curve from this work results in a higher response than that modeled using the Marmottant model at driving pressures below 50 kPa, see Fig. 7C. The effect of the initial surface tension on the total relative amplitude of oscillation at the second harmonic , $\int_{0.7\ MHz}^{4\ MHz} \varepsilon_{2H} df$, is plotted in Fig. 7D. It shows that the difference in the second harmonic response is mainly attributed to lower resistance against expansion as compared to that against compression. This can be concluded from the observed difference at the higher initial surface tensions, starting at $\sigma(R_0) \approx 20$ mN/m, where the shell elasticity is lower during the expansion phase than during the compression phase. Further experimental research involving non-linear scattering is required to investigate the nonlinear dynamics in more detail and to validate the results of the modeling effort.

Finally, it is of interest to discuss the maximum value of the shell elasticity of 0.6 N/m found in this work. In literature, a broad range of shell elasticity values have been reported. For DPPC based bubbles the reported values range from 0.06 N/m[55] up to approx. 2.5 N/m.[19,37,56,57] For DSPC based bubbles the lower limit of χ is similar to that of DPPC based bubbles however, even higher maximum values have been reported, up to 3.5 N/m.[20,38,58] To date, the nature of the reported differences remains unclear. The length of the PEG chain, the length of the primary lipid molecules, temperature, microbubble production method, resting time after synthesis, and phase behavior and microstructure formation of the lipids in the coating may all play a role.[59–61] Furthermore, acoustically driven selective loss of shell components may influence shell stiffness. In our previous work, it was shown that the shell elasticity of monodisperse microbubbles formed by flow-focusing and coated by a very similar lipid mixture (DPPC:DPPA:DPPE-PEG5k, 8:1:1 molar ratio) can increase from 0.8 N/m to 2.5 N/m during multiple acoustic insonations[28] which, in part, can now be explained from a slight (2%) decrease in bubble radius due to acoustically driven dissolution. Nevertheless, in the present work, the maximum shell stiffness measured upon bubble compression was only 0.6 N/m and therefore, the previously obtained high shell stiffness of our previous work cannot be fully explained from the present results and another physical microstructure and/or underlying mechanism must be at play. All in all, future work is necessary to develop a universal understanding of the physicochemical- and acoustic parameters that determine shell elasticity, e.g. using monodisperse bubbles with a well defined response and the novel elasticity characterization method presented here.

5 Conclusions

The dilatational elasticity and corresponding dilatational interfacial tension of lipid-coated monodisperse microbubbles can be measured at high precision using acoustic attenuation measurements at controlled ambient pressures. For monodisperse C_4F_{10} filled microbubbles coated with DPPC and DPPE-PEG5000 mixed at molar fractions of 5.0%, 7.5%, and 10.0%, the surface elasticity is highly dependent on the dilatation of the bubble surface. During bubble compression, the elasticity increases up to an elasticity of 0.6 N/m at which the monolayer collapses and the elasticity vanishes. During bubble expansion, the elasticity first monotonically drops to an elasticity of 0.35 N/m, after which it more rapidly drops to zero. No difference was observed in the elasticity-area curves obtained for bubbles of a different size, and for the bubbles coated with different PEG molar shell fractions. The elasticity-area curves were integrated with respect to the microbubble surface area to find the dilatational interfacial tension of DPPC/DPPE-PEG5000 coated microbubbles. Upon expansion, the interfacial tension increases, first rapidly, and then more slowly from zero to the surface tension of the surrounding medium. Thus, we showed by direct experimental evidence that indeed, a phospholipid-coated microbubble is in a tensionless state when it is compressed, and, that it has the interfacial tension of the surrounding medium upon expansion. The novel measurement technique presented in this work revealed the detailed features of the nonlinear interfacial shell behavior of micrometer sized bubbles coated with phospholipids.

Acknowledgements

Anne Lassus is kindly acknowledged for the preparation of the lipid dispersions. We thank Brandon Helfield for stimulating discussions. Finally, we thank Thierry Bettinger for his support to the project.

Appendix

The average of the measured $\sigma(A/A_N)$ curves shown in Fig. 5C was parametrized by a 10th degree polynomial fit in Matlab. The high order polynomial fit was chosen to capture all the details of the measured $\sigma(A/A_N)$ curve. The parametrization was performed as follows:

$$\begin{aligned} \sigma_{fit}\left(\tfrac{A}{A_N}\right) &= 0 && \text{if } A_m < 0.92 \\ \sigma_{fit}\left(\tfrac{A}{A_N}\right) &= \textstyle\sum_{n=0}^{10} 10^{10} c_n A_m^n, && \text{if } 0.92 \le A_m \le 1.12 \\ \sigma_{fit}\left(\tfrac{A}{A_N}\right) &= \sigma_w && \text{if } A_m > 1.12 \end{aligned} \tag{11}$$

where $A_m = A/A_N$. A_N can have a different value than the bubble surface area at atmospheric pressure A_0 in order to control the initial surface tension $\sigma(A_0)$. The coefficients of the polynomial fit are given in Table 1.

Table 1 Coefficients of the 10th degree polynomial fit to the average of the measured $\sigma(A/A_N)$ curves.

c_0	c_1	c_2	c_3	c_4	c_5	c_6	c_7
-0.04	0.39	-1.70	4.47	-7.69	9.10	-7.41	4.16
c_8	c_9	c_{10}					
-1.53	0.33	-0.03					

Notes and references

1 N. de Jong, R. Cornet and C. Lancée, *Ultrasonics*, 1994, **32**, 447.

2 M. Overvelde, V. Garbin, J. Sijl, B. Dollet, N. de Jong, D. Lohse and M. Versluis, *Ultrasound Med. Biol.*, 2010, **36**, 2080–2092.

3 J. R. Lindner, *Nat. Rev. Drug Disc.*, 2004, **3**, 527–533.

4 T. G. Leighton, *The Acoustic Bubble*, Academic Press, 1994.

5 S. Paul, A. Katiyar and K. Sarkar, *J. Acoust. Soc. Am.*, 2010, **127**, 3846–3857.

6 N. de Jong and L. Hoff, *Ultrasonics*, 1993, **31**, year.

7 S. van der Meer, B. Dollet, M. Voormolen, C. T. Chin, A. Bouakaz, N. de Jong, M. Versluis and D. Lohse, *J. Acoust. Soc. Am.*, 2007, **121**, 648–656.

8 H. Mohwald, *Handbook of Biological Physics*, Elsevier Science, Amsterdam, 1995.

9 R. Glazman, *J. Acoust. Soc. Am.*, 1983, **74**, 980–986.

10 K. Sarkar, W. T. Shi, D. Chatterjee and F. Forsberg, *J. Acoust. Soc. Am.*, 2005, **118**, 539 – 550.

11 P. Marmottant, S. Van Der Meer, M. Emmer, M. Versluis, N. De Jong, S. Hilgenfeldt and D. Lohse, *J. Acoust. Soc. Am.*, 2005, **118**, 3499 – 3505.

12 J. Sijl, M. Overvelde, B. Dollet, V. Garbin, N. de Jong, D. Lohse and M. Versluis, *J. Acoust. Soc. Am.*, 2011, **129**, 1729–1739.

13 P. J. A. Frinking, E. Gaud, J. Brochot and M. Arditi, *IEEE Trans. Ultrason. Ferroelec. Freq. Contr.*, 2010, **57**, 1762 – 1771.

14 J. Sijl, B. Dollet, M. Overvelde, V. Garbin, T. Rozendal, N. de Jong, D. Lohse and M. Versluis, *J. Acoust. Soc. Am.*, 2010, **128**, 3239–3252.

15 M. M. Lozano and M. L. Longo, *Soft Matter*, 2009, **5**, 1822–1834.

16 S. Lee, D. H. Kim and D. Needham, *Langmuir*, 2001, **17**, 5544–5550.

17 A. P. Kotula and S. L. Anna, *Soft Matter*, 2016, **12**, 7038–7055.

18 N. Alvarez, L. Walker and S. L. Anna, *Langmuir*, 2010, **26**, 13310?13319.

19 D. E. Goertz, N. de Jong and A. F. W. van der Steen, *Ultrasound Med. Biol.*, 2007, **33**, 1376–1388.

20 T. Segers, N. de Jong and M. Versluis, *J. Acoust. Soc. Am.*, 2016, **140**, 2506–2517.

21 M. Emmer, H. J. Vos, D. E. Goertz, A. van Wamel, M. Versluis and N. de Jong, *Ultrasound Med. Biol.*, 2009, **35**, 102–111.

22 J. A. Feshitan, C. C. Chen, J. J. Kwan and M. A. Borden, *J. Coll. Interf. Sci*, 2009, **329**, 316–324.

23 M. P. Kok, T. Segers and M. Versluis, *Lab. Chip*, 2015, **15**, year.

24 T. Segers and M. Versluis, *Lab. Chip*, 2014, **14**, 1705–1714.

25 A. M. Gañán-Calvo and J. M. Gordillo, *Phys. Rev. Lett.*, 2001, **87**, 274501.

26 S. L. Anna, N. Bontoux and H. A. Stone, *Appl. Phys. Lett.*, 2003, **82**, 364–366.

27 P. Garstecki, H. A. Stone and G. M. Whitesides, *Phys. Rev. Lett.*, 2005, **94**, 164501.

28 T. Segers, L. de Rond, N. de Jong, M. Borden and M. Versluis, *Langmuir*, 2016, **32**, 3937–3944.

29 K. Hettiarachchi, E. Talu, M. L. Longo, P. A. Dayton and A. P. Lee, *Lab. Chip*, 2007, **7**, 463–468.

30 E. Talu, K. Hettiarachchi, R. J. Powell, A. P. Lee, P. A. Dayton and M. L. Longo, *Langmuir*, 2008, **24**, 1745–1749.

31 T. Segers, D. Lohse, M. Versluis and P. Frinking, *Langmuir*, 2017, **33**, 10329–10339.

32 *Daniel Blair, Eric Dufresne*, `http://glinda.lrsm.upenn.edu/~weeks/idl`.

33 A. Prosperetti, *J. Acoust. Soc. Am.*, 1976, **61**, 17–27.

34 N. de Jong, L. Hoff, T. Skotland and N. Bom, *Ultrasonics*, 1992, **30**, 95–103.

35 K. Commander and A. Prosperetti, *J. Acoust. Soc. Am.*, 1989, **85**, 731–746.

36 L. Hoff, P. Sontum and J. Hovem, *J. Acoust. Soc. Am.*, 2000, **107**, 2272–2280.

37 T. Faez, D. Goertz and N. de Jong, *Ultrasound Med. Biol.*, 2010, **37**, 338–342.

38 J. M. Gorce, M. Arditi and M. Schneider, *Ivestigative Radiology*, 2000, **35**, 661–671.

39 Y. Luan, G. Lajoinie, E. Gelderblom, I. Skachkov, A. F. W. van der Steen, H. J. Vos, M. Versluis and N. de Jong, *Ultrasound Med. Biol.*, 2014, **40**, 1834–1846.

40 J. O'Brien, N. Ovenden and E. Stride, *J. Acoust. Soc. Am.*, 2011, **130**, 180–185.

41 T. Segers, P. Kruizinga, M. Kok, G. Lajoinie, N. de Jong and M. Versluis, *Ultrasound Med. Biol.*, 2018, **https://doi.org/10.1016/j.ultrasmedbio.2018.03.019**,.

42 J. J. Kwan and M. A. Borden, *Soft Matter*, 2012, **8**, 4756–4766.

43 A. Katiyar, K. Sarkar and P. Jain, *Journal of Colloid and Interface Science*, 2009, **336**, 519–525.

44 M. A. Borden and M. L. Longo, *Langmuir*, 2002, **18**, 9225–9233.

45 S. Dicker, M. Mleczko, M. Siepmann, N. Wallace, Y. Sunny, C. R. Bawiec, G. Schmitz, P. Lewin and S. P. Wrenn, *Ultrasound Med. Biol.*, 2013, **39**, 1292–1302.

46 K. Morgan, J. Allen, P. Dayton, J. Chomas, A. Klibanov and K. Ferrara, *IEEE Trans. Ultrason. Ferroelectr. Freq. Control*, 2000, **47**, 1494–1509.

47 J. Tu, J. Guan, Y. Qiu and T. J. Matula, *J. Acoust. Soc. Am.*, 2009, **126**, 2954–2962.

48 M. Vranceanu, K. Winkler, H. Nirschl and G. Leneweit, *Biophysical Journal*, 2088, **94**, 3924–3934.

49 J. Krägel, J. Li, R. Miller, M. Bree, G. Kretzschmar and H. Möhwald, *Colloid Polym. Sci.*, 1996, **274**, 1183–1187.

50 K. N. Kumar and K. Sarkar, *Ultrasound Med. Biol.*, 2016, **42**, 1010–1017.

51 K. N. Kumar and K. Sarkar, *J. Acoust. Soc. Am.*, 2015, **138**, 624–634.

52 A. a. Doinikov, S. Zhao and P. a. Dayton, *Ultrasonics*, 195–201.

53 M. Tang, R. Eckersley and J. Noble, *Ultrasound Med. Biol.*, 2005, **31**, 377–384.

54 L. Xia, M. T. Porter and K. Sarkar, *J. Acoust. Soc. Am.*, 2015, **138**, 3994–4003.

55 T. van Rooij, Y. Luan, G. Renaud, A. van der Steen, M. Versluis, N. de Jong and K. Kooiman, *Ultrasound Med. Biol.*, 2015, **41**, 1432 –1445.

56 B. L. Helfield and D. E. Goertz, *J. Acoust. Soc. Am.*, 2013, **133**, 1158–1168.

57 J. Lum, D. Stobbe, M. Borden and T. Murray, *Appl. Phys. Lett.*, 2018, **112**, 111905.

58 J. Lum, J. Dove, T. Murray and M. Borden, *Langmuir*, 2016, **32**, 9410–9417.

59 M. A. Borden and M. L. Longo, *Journal of Physical Chemistry*, 2004, **108**, 6009–1344.

60 A. Thomas and M. Borden, *Langmuir*, 2017, **33**, 13699–13707.

61 K. Kooiman, T. Van Rooij, B. Qin, F. Mastik, H. Vos, M. Versluis, A. Klibanov, N. de Jong, F. Villanueva and X. Chen, *PloS one*, 2017, **12**, e0180747.